Computers & Fluids 83 (2013) 3–14

Contents lists available at SciVerse ScienceDirect

Computers & Fluids

journal homepage: www.elsevier.com/locate/compfluid

Enhancement of Lagrangian slide lines as a combined force and velocity boundary condition

M. Kuchařík [a,*], R. Loubère [b], L. Bednárik [a], R. Liska [a]

[a] FNSPE, Czech Technical University in Prague, Břehová 7, 115 19 Praha 1, Czech Republic
[b] Institut de Mathématiques de Toulouse, CNRS, Université de Toulouse, France

ARTICLE INFO

Article history:
Received 14 November 2011
Received in revised form 1 June 2012
Accepted 3 June 2012
Available online 15 June 2012

Keywords:
Lagrangian hydrodynamics
Slide lines
Staggered scheme

ABSTRACT

Many hydrodynamical problems involve shear flows along material interfaces. If the materials move along each other but are tied to a single Lagrangian computational mesh without any sliding treatment, severe mesh distortions appear which can eventually cause the failure of the simulation. This problem is usually treated by introducing the sliding line framework into the Lagrangian code. In this paper, we revise the 2D approach described in the article E.J. Caramana, *The implementation of slide lines as a combined force and velocity boundary condition*, Journal of Computational Physics 228 (2009), and suggest two enhancements – interpolated interaction instead of a simple one-to-one interaction described in the previous article, and a numerical surface tension model improving the stability of the interface. Both improvements stabilize the slide line and lead to more realistic results, as shown on selected numerical examples.

1. Introduction

In realistic physical simulations, people often face problems of shear flows at material interfaces. If the materials move along each other but are tied to a single computational mesh without any sliding treatment, severe distortions appear which can eventually cause the failure of the simulation. A typical example is the motion of a laser produced plasma in a deforming channel [1], or a shear flows in a high-velocity impact problem [2]. One option to solve this problem is the introduction of a slide line environment into the Lagrangian code.

The demand for a slide line treatment arose when first realistic Lagrangian simulations became attractive. Generally, all sliding algorithms can be classified into two groups [3,4]. The first group, in which the overall forces between the sides of the slide line are computed, includes popular methods of Lagrangian multipliers [5,6] or the penalty method [7]. We focus here on the second type of methods, where quantities are mapped across the slide line and the nodes are treated in a similar manner as the internal nodes. The introduction of slide lines is an old but fruitful idea that dates back to Wilkins [8] as a chapter in a book (reproduced in Chapter 5 of Wilkins [9]). In this approach, the interaction of both sides of the slide line is explicitly calculated, and their inter-penetration is prevented by an explicit put-back-on step. This approach is very popular and is used for slide line treatment in many hydrodynamic codes. There exist many modifications of this approach, see for example [10–12]. For an overview of the slide line algorithms see the specialized report [13] or the classical more general paper [4].

Another possibility to treat sliding lines in a compatible staggered Lagrangian code [14] is a special type of boundary condition for nodal forces and velocities. Suppose that there exist two different meshes interacting with each other through a common sliding line, one of them is specified as the master side defining the slide line shape, while the other – slave – side follows the slide line. We keep the main idea of Caramana [15] and incorporate the contact forces for the nodes on the slide line, representing the forces due to the pressure gradient across the interface. The second main ingredient of the sliding line treatment is the correction preventing the inter-penetration of two sides. This is the main difference between the two approaches. In [9], the inter-penetration is prevented by an explicit put-back-on step in which the slave nodes are artificially moved back onto the master slide line edges. Instead of this artificial nodal motion, the velocity correction is used [15]. The correction is simpler and compatible with the rest of the Lagrangian solver.

In this paper, we focus on the sliding mechanism in the purely hydrodyamic situation. We describe the method from Ref. [15] with details, some of which are eluded in the original paper. In [15], the nodes on the slide line exclusively interact with one mesh node from the other side of the slide line, and this interaction can cause severe distortions of the interface. We suggest here the improvement in which the interaction is performed in an interpolated sense. Moreover, as the shear flow (sliding) is present here, the original method can result in interface disturbances due to

* Corresponding author.
E-mail address: kucharik@newton.fjfi.cvut.cz (M. Kuchařík).

0045-7930/$ - see front matter © 2012 Elsevier Ltd. All rights reserved.
http://dx.doi.org/10.1016/j.compfluid.2012.06.005

evolving (real or numerical) Kelvin–Helmholtz instabilities. To stabilize the interface, we suggest here a type of numerical surface tension model preventing the instability to appear. We skip all issues related to void opening or closing, which may be very important for the practical computations, however this topic will be treated in future investigations.

The rest of the paper is organized as follows. In Section 2, we briefly describe the staggered Lagrangian hydrodynamics which we use to derive and test the slide line framework. In Section 3, the slide line treatment from Ref. [15] is reviewed and explained in detail. In Section 4, we suggest the interpolated interaction, changing the communication between the nodes on both sides of the slide line from one-to-one to interpolated. In Section 5, another improvement is suggested, the numerical surface tension, eliminating evolution of the Kelvin–Helmholtz instability due to the shear flow along the interface. The behavior of the improved method and its comparison with the original method on selected numerical tests is performed in Section 6. Finally, the whole paper is concluded in Section 7.

2. Staggered Lagrangian hydrodynamics

In the Lagrangian framework, the gas dynamics equations can be written in the following form,

$$\rho \frac{d}{dt}\left(\frac{1}{\rho}\right) - \nabla \cdot \vec{v} = 0, \tag{1}$$

$$\rho \frac{d}{dt}\vec{v} + \nabla P = \vec{0}, \tag{2}$$

$$\rho \frac{d}{dt}\varepsilon + P\nabla \cdot \vec{v} = 0, \tag{3}$$

where ρ is the fluid density, $\vec{v}$ is the velocity, ε the specific internal energy, and $\frac{d}{dt}$ denotes the total Lagrangian time derivative. The first equation expresses the volume conservation equation, whereas the second and third ones are the momentum and total energy conservation equations. Volume conservation equation is often referred to as the Geometric Conservation Law (GCL). The previous system is supplemented by a thermodynamics closure (equation of state – EOS), $P = P(\rho, \varepsilon)$. Often, the ideal gas equation of state is used, $p = (\gamma - 1)\rho\varepsilon$, where γ is the ratio of specific heats. The last equations are the trajectory equations

$$\frac{d\vec{x}}{dt} = \vec{v}(\vec{x}(t), t), \tag{4}$$

expressing the Lagrangian motion of any point located at position $\vec{x}$.

We use a staggered placement of variables in which position and velocity are defined at mesh nodes while thermodynamic variables (density, pressure, energy) are located at cell centers. We denote the computational zone (cell) by the symbol z, mesh points (nodes) are denoted by the symbol p. Following the compatible discretization from Ref. [14], the mass of zone z is connected with the mass of the adjacent point p by the notion of the subzonal masses, m_{zp},

$$m_z = \sum_{p \in P(z)} m_{zp}, \quad m_p = \sum_{z \in Z(p)} m_{zp}, \tag{5}$$

where $P(z)$ stands for the set of points in zone z, and $Z(p)$ stands for the set of zones adjacent to point p. The subzones are assumed to be Lagrangian entities, which implies that the subzonal masses are initialized at the beginning of the simulation, $m_{zp} = \rho_{zp} V_{zp}$ and remain constant in time, implying that cell and nodal masses remain constant either.

The discrete trajectory equation for mesh nodes can be written as

$$\frac{d\vec{x}_p}{dt} = \vec{v}_p, \tag{6}$$

which together with the assumption of constant cell mass guarantees satisfaction of the GCL Eq. (1). The momentum Eq. (2) can be written in the semi-discrete form for a particular mesh point p,

$$m_p \frac{d\vec{v}_p}{dt} = \vec{F}_p, \tag{7}$$

where the Newton force is computed by evaluating the pressure gradient in the dual cell Ω_p corresponding to node p (union of subzones adjacent to p),

$$\vec{F}_p = -\int_{\Omega_p} \vec{\nabla} P dV = -\sum_{z \in Z(p)} \int_{\Omega_{zp}} \vec{\nabla} P dV = \sum_{z \in Z(p)} \vec{F}_{zp}, \tag{8}$$

where the subzonal forces $\vec{F}_{zp}$ are evaluated by transforming the volume integrals to boundary integrals using the Green divergence theorem. Finally, following [14], the semi-discrete form of the energy Eq. (3) can be written as

$$m_z \frac{d\varepsilon_z}{dt} = -\sum_{p \in P(z)} \vec{F}_{zp} \cdot \vec{v}_p, \tag{9}$$

which is derived from the total energy conservation on a cell-by-cell basis. This approach is supplemented by additional forces representing artificial viscosity [16] and anti-hourglass mechanism [17], stabilizing the solution and preventing the simulation from failure. The update of fluid specific internal energy and velocity come from the finite difference discretization of Eqs. (7) and (9), new nodal positions from Eq. (6), new fluid density is obtained by dividing the constant cell mass by the new cell volume, and new pressure from the EOS. For a full description of the compatible Lagrangian scheme including more details, such as timestep control of predictor–corrector time integration scheme, see [14,16,17].

3. Slide line treatment

Quoting Caramana [15]: "Slide lines (2D) and surfaces (3D) are a way to treat interfaces in Lagrangian hydrocodes that allow different materials or regions to move relative to each other without the grid distortion that would otherwise terminate these calculations quickly." The presence of fluid instabilities is often, if not always, a cause of failure for Lagrangian codes. The idea of slide lines comes from Ref. [8], and was reproduced in Chapter 5 of Wilkins [9]. By all means most of slide line treatments follow this original work of Wilkins as pointed by Caramana [15]. Slide line is an important feature although it is quite rarely described.

Any method treating slide lines in a Lagrangian hydrocode must ideally respect some general requirements. On the first hand some requirements are related to the properties of the physical underlying system and the Lagrangian numerical scheme used to solve it. As instance conservation of mass, momentum and total energy obeyed by the physical system and the numerical scheme must be also preserved by the specific slide line treatment. The normal acceleration between two materials being continuous, the slide line treatment is required to preserve such continuity. In addition the slide line treatment must not destabilize steady solutions (as instance homogeneous fluids with constant pressure and velocity field). Over and above ideal situations must be perfectly dealt with independently of the possibly different mesh sizes across the slide line. More precisely fake slide lines must have an ignorable impact, straight slide line must remain so in pure sliding situations. On the other hand some requirements are related to the physics involved at the slide line. As instance two materials sliding on each other never inter-penetrate, consequently the slide line treatment should also obey this principle. Furthermore the resulting contact

force between two sliding materials must only act in the normal direction to the slide line. In addition, in the frictionless case, the tangential net force due to the contact must be zero.

Developing a slide line algorithm demands to, exactly or approximately, fulfill these requirements. The technique developed in [15] and described in Section 3.1 first determines scaled contact forces normal to the slide line. Apart from momentum conservation (for non-ideal cases) and inter-penetration problem the technique fulfills the previous requirements. Contact forces are determined by trying to perfectly deal with ideal situations. Then, to ensure that no penetration occurs, the point velocity on one side of the slide line is further corrected in Section 3.2. Unfortunately, doing so, the technique slightly losses total energy conservation. Nonetheless such energy discrepancy is used to assess the meaningfulness of the computation, see Section 3.3.

3.1. Contact forces

The first task is to determine the contact force for the ideal situation as shown in Fig. 1 where a computational mesh is split in two parts separated by a single slide line splitting each point on the slide line into two half-points p and p'. Here the design principle consists of exactly retrieving the momentum Eq. (7) for one point when the slide line splits (7) in two equations for two half-points,

$$m_p \frac{d\vec{v}_p}{dt} = \vec{F}_p + \vec{g}_p, \quad m_{p'} \frac{d\vec{v}_{p'}}{dt} = \vec{F}_{p'} + \vec{g}_{p'}, \tag{10}$$

where $\vec{F}_p$ and $\vec{F}_{p'}$ represent the sum of subzonal forces from lower/upper subzones attached to the half-points and their sum is equal to the original total nodal force, and similarly with the masses of the half-points m_p and $m_{p'}$. Moreover, $\vec{g}_p/\vec{g}_{p'}$ represent the contact forces acting on the lower/upper half-point from the opposite side of the slide line. When we assume that p and p' coincide and have the same mass and geometry, the separate Eq. (10) have to sum to the original Eq. (7) which implies $\vec{g}_{p'} = -\vec{g}_p$. After substituting this back to (10) and assuming the same acceleration for both half-points, the contact forces become

$$\vec{g}_p = -\vec{g}_{p'} = \frac{m_p \vec{F}_{p'} - m_{p'} \vec{F}_p}{m_p + m_{p'}}. \tag{11}$$

Let us move to a less ideal situation shown in Fig. 2a where both sides of the slide line remain straight, however, the cell aspect ratios are different. In this case one defines the outer normals for each edge on a slide line, $\vec{N}$, which have the normal directions, and their size is defined by the length of the edge. The nodal outer normal is defined (as suggested in [15]) by the average of the adjacent edge normals,

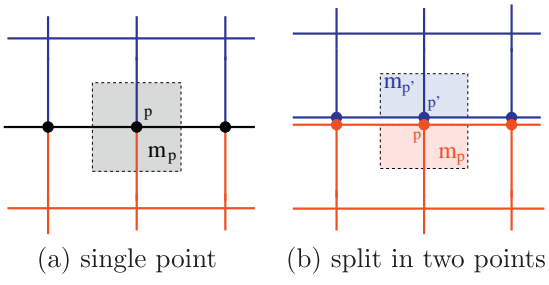

Fig. 1. (a) One point in a mesh separated in its lower (red) and upper (blue) part by imaginary slide line (black line). One particular point p is shown with its dual cell containing the corresponding nodal volume/mass m_p (gray rectangle). (b) Point separated to two half-points p and p', belonging to different sides of the slide line. (For interpretation of the references to color in this figure legend, the reader is referred to the web version of this article.)

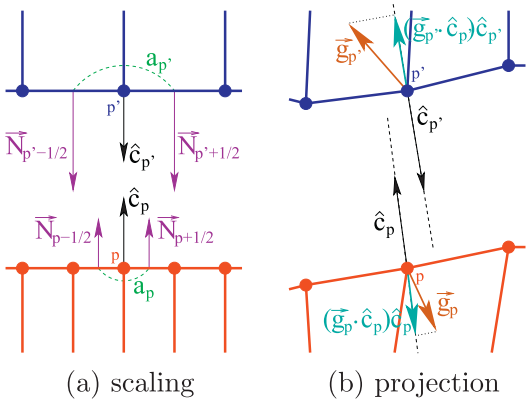

Fig. 2. (a) Definition of edge outer normals $\vec{N}_{p\pm1/2}$, nodal unit normals $\hat{c}_p$, and nodal characteristic lengths a_p. (b) Projection of contact forces $\vec{g}_p$ to the normal direction a_p.

$$\vec{N}_p = \left(\vec{N}_{p-\frac{1}{2}} + \vec{N}_{p+\frac{1}{2}}\right)/2, \tag{12}$$

where $p-1/2$ and $p+1/2$ denote the left and right edges in the slide line with respect to point p. The characteristic size a_p of node p is defined as $a_p = \|\vec{N}_p\|$ which corresponds to the length between the edge centers of the two adjacent edges. The nodal unit normal is defined as $\hat{c}_p = \vec{N}_p/a_p$.

Because two upper cells sharing one single node p' interact with possibly more than two lower cells we need to "impedance" match the force interactions across the slide line. (In other words an interaction area $a_{p'}$ of point p' must be matched by an approximately equal area of interaction from the opposite side no matter how many points p from this opposite side contribute.)

When p and p' coincide as in Fig. 2a it is somewhat enlightening to consider the "meta-cell" constituted of some part of the upper cells sharing point p' and the lower cells associated to the interaction area a_p. In this meta-cell the mass of point $p \equiv p'$ is approximately given by $m_p + m_{p'}\frac{a_p}{a_{p'}}$ because, if one assumes that $m_{p'}/a_{p'}$ represents the density of the mass along lower boundary cells, then $m_{p'}\frac{a_p}{a_{p'}}$ does represent the approximate mass related to the interaction area a_p. In the same way the acceleration of $p \equiv p'$ in the meta-cell may be approximated by $\left(\vec{F}_p + \vec{F}_{p'}\frac{a_p}{a_{p'}}\right)\Big/\left(m_p + m_{p'}\frac{a_p}{a_{p'}}\right)$.

The half-sided momentum equations are given by

$$m_p \frac{d\vec{v}_p}{dt} = \vec{F}_p + \vec{G}_p, \quad m_{p'} \frac{d\vec{v}_{p'}}{dt} = \vec{F}_{p'} + \vec{G}_{p'}, \tag{13}$$

where $\vec{G}_p = (\vec{g}_p \cdot \hat{c}_p)\hat{c}_p$ and $\vec{G}_{p'} = (\vec{g}_{p'} \cdot \hat{c}_{p'})\hat{c}_{p'}$ are the normal component of the contact forces. The contact force is then defined as the normal component of the acceleration of the point in the meta-cell, that is to say $\vec{G}_p$ force is determined as the solution of

$$\frac{d\vec{v}_p}{dt} \cdot \hat{c}_p = \frac{\vec{F}_p + \vec{G}_p}{m_p} \cdot \hat{c}_p \equiv \frac{\vec{F}_p + \vec{F}_{p'}\frac{a_p}{a_{p'}}}{m_p + m_{p'}\frac{a_p}{a_{p'}}} \cdot \hat{c}_p, \tag{14}$$

leading to $\vec{g}_p \cdot \hat{c}_p = \frac{m_p(\vec{F}_{p'}\cdot\hat{c}_p) - m_{p'}(\vec{F}_p\cdot\hat{c}_p)}{a_{p'}m_p + a_p m_{p'}} a_p$. We further approximate the projected force by the projection to the normal from the opposite side, $\vec{F}_{p'} \cdot \hat{c}_p \approx -\vec{F}_{p'} \cdot \hat{c}_{p'}$ to get

$$\vec{g}_p \cdot \hat{c}_p \approx -\frac{m_p\left(\vec{F}_{p'} \cdot \hat{c}_{p'}\right) + m_{p'}\left(\vec{F}_p \cdot \hat{c}_p\right)}{a_{p'}m_p + a_p m_{p'}} a_p. \tag{15}$$

As a consequence $\vec{G}_p$ (and $\vec{G}_{p'}$ following the same logic) is determined by

$$\vec{G}_p = (\vec{g}_p \cdot \hat{c}_p)\hat{c}_p \approx -\frac{m_p\left(\vec{F}_{p'} \cdot \hat{c}_{p'}\right) + m_{p'}\left(\vec{F}_p \cdot \hat{c}_p\right)}{a_{p'}m_p + a_p m_{p'}} a_p \hat{c}_p, \tag{16}$$

$$\vec{G}_{p'} = (\vec{g}_{p'} \cdot \hat{c}_{p'})\hat{c}_{p'} \approx -\frac{m_{p'}\left(\vec{F}_p \cdot \hat{c}_p\right) + m_p\left(\vec{F}_{p'} \cdot \hat{c}_{p'}\right)}{a_p m_{p'} + a_{p'} m_p} a_{p'} \hat{c}_{p'}. \tag{17}$$

Both formulas are the same up to a prime sign again. The projection is demonstrated in Fig. 2b. When the points p and p' do not coincide then the meta-cell construction is only an approximation, so are the point mass and its acceleration.

By construction two of the previously listed requirements, namely the contact force acting only in the normal direction and the frictionless requirement, are obeyed. Moreover the normal acceleration between the two materials is continuous because $\frac{1}{m_p}(\vec{F}_p + \vec{G}_p) \cdot \hat{c}_p = -\frac{1}{m_{p'}}(\vec{F}_{p'} + \vec{G}_{p'}) \cdot \hat{c}_{p'}$. While the momentum conservation is not ensured to round-off error for non-ideal situations it is still conserved to truncation error when summed over all of the points of the slide line.[1] On the other hand total energy conservation is preserved because the slide line treatment is so far expressed as contact forces which are further participating in the internal energy update (9) relying on the compatible construction of the numerical scheme. Furthermore we have obtained equations (16) and (17) by requiring the slide line algorithm to retrieve ideal situations; Areas a are used to scale the G quantities so that we obtain the "exact" result given by (11) in the limit of exactly the same number of aligned grid points on both sides of the slide line. Lastly we can verify that the slide line treatment maintains a constant pressure even when non-uniform meshes are used, see also the numerical experiments on pure sliding situations in Section 6.1.

Unfortunately the slide line treatment does not prevent the two sides to inter-penetrate. The contact force is constructed to avoid such an unlikely situation to occur, however, there is no intrinsic mechanism that can prevent it. The next section presents the velocity correction technique [15] to prevent inter-penetration.

3.2. Velocity correction preventing inter-penetration

Up to now, the slide line has been treated in a symmetric manner concerning the upper and lower sides. However, classical treatment of slide line defines a "master" and "slave" side. In general, the materials on both sides dictate such dichotomy. Without loss of generality, let us assume that the lower (red[2]) side in our figures is declared as slave. Because inter-penetration can occur the slave side of the slide line is forced to follow the master side – the so-called "put-back-on step" puts back any point from the slave side onto the master side [9].

The last ingredient proposed by Caramana [15] relates to this put-back-on step. In fact, the solution of the inter-penetration problem is recast into a velocity boundary condition. More precisely, the update of velocity of slide points coming from (13) is given by

$$\vec{v}_p^{n+1,\dagger} = \vec{v}_p^n + \frac{\Delta t}{m_p}\left(\vec{F}_p + \vec{G}_p\right), \quad \vec{v}_{p'}^{n+1,\dagger} = \vec{v}_{p'}^n + \frac{\Delta t}{m_{p'}}\left(\vec{F}_{p'} + \vec{G}_{p'}\right). \tag{18}$$

The final master velocity is not modified, i.e. $\vec{v}_{p'}^{n+1} = \vec{v}_{p'}^{n+1,\dagger}$, while the slave velocity is altered to

$$\vec{v}_p^{n+1} = \vec{v}_p^{n+1,\dagger} + \left[\left(\vec{v}_{p'}^{n+1,\dagger} + \vec{v}_{p'}^n\right) \cdot \hat{c}_{p'}\right]\hat{c}_{p'} - \left[\left(\vec{v}_p^{n+1,\dagger} + \vec{v}_p^n\right) \cdot \hat{c}_{p'}\right]\hat{c}_{p'}, \tag{19}$$

which guarantees that the projection of the time centered velocities $\vec{v}_{p'}^{n+1/2} = (\vec{v}_{p'}^{n+1} + \vec{v}_{p'}^n)/2$, $\vec{v}_p^{n+1/2} = (\vec{v}_p^{n+1} + \vec{v}_p^n)/2$ on the normal $\hat{c}_{p'}$ coincide, i.e. $\vec{v}_{p'}^{n+1/2} \cdot \hat{c}_{p'} = \vec{v}_p^{n+1/2} \cdot \hat{c}_{p'}$. In words, this slave velocity correction removes the excessive velocity in the direction of inter-penetration (slide line normal) from the final velocity. Consequently, this correction prevents the slave node to move in this direction more than the corresponding master node does. This correction is weaker than the explicit put-back-on step [9] and does not bring so strong disturbance into the compatible Lagrangian schemes. While this velocity correction provides a way to fulfill the inter-penetration requirement it also affects the energy conservation as this small correction is not recast into the compatible formulation.

3.3. Energy discrepancy

In the context of a compatible Lagrangian scheme and away from boundary conditions the total energy is conserved up to machine precision. During one time step $\Delta t = t^{n+1} - t^n$, internal energy in zone z changes as

$$m_z(\varepsilon_z^{n+1} - \varepsilon_z^n) = -\sum_{p \in P(z)} \vec{F}_p^z \cdot \Delta\vec{r}_p, \tag{20}$$

where $\Delta\vec{r}_p = \Delta t\left(\vec{v}_p^{n+1} + \vec{v}_p^n\right)/2$ represents nodal motion during the time step. Kinetic energy in point p changes as

$$\frac{1}{2}m_p\left(\left(\vec{v}_p^{n+1}\right)^2 - \left(\vec{v}_p^n\right)^2\right). \tag{21}$$

Due to compatibility of the scheme, both energy changes summed over the entire mesh should be the same. However, the presence of a slide line may interfere with this equilibrium. The sliding forces are naturally treated by the energy update of the compatible scheme, but the velocity correction can introduce some discrepancy in the energy conservation. In [15] the author presents a way to measure this discrepancy. The work done by the slide line on a time step Δt upon a point p of the slide line is computed as

$$\Delta W_p^{n,n+1} = \left[\frac{1}{2}m_p\left((\vec{v}_p^{n+1})^2 - (\vec{v}_p^n)^2\right)\right] - \left[\sum_{z \in Z(p)} \vec{F}_p^z \cdot \Delta\vec{r}_p\right], \tag{22}$$

where the internal energy change was transformed from a sum over cells to a sum over nodes. By construction of the compatible scheme, the total energy E is conserved, but the work done by the slide line remains so that

$$E^{n+1} - E^n = \sum_{p \text{ in slide line}} \Delta W_p^{n,n+1}. \tag{23}$$

To compute the overall energy discrepancy during the entire simulation, one can accumulate over time,

$$E^{n+1} - E^0 = \sum_{i=1}^{n+1} \sum_{p \text{ in slide line}} \Delta W_p^{i-1,i}. \tag{24}$$

This last equation represents the total energy discrepancy brought into the simulation due to the velocity correction of the slide line treatment.

4. Interpolated interaction

The approach [15] described in the previous section employs the standard point-to-point interaction where the pressure forces $\vec{F}$, velocities $\vec{v}$, characteristic lengths a_p, and the outer normals $\hat{c}$ on the opposite side of the slide line are simply taken from the nearest opposite point. This approach works reasonably well and it is the best choice from the parallelization point of view, however, it can lead to staircase-shape of the slide line when different aspect

[1] Indeed let us remark that in the case the normals are collinear and opposite, $\hat{c}_p = -\hat{c}_{p'}$, the sum of $\vec{G}_p/a_p$ and $\vec{G}_{p'}/a_{p'}$ (make the force intensive with respect to a's) is identically zero. With the normals being different there is again an error at truncation level because of the curvature along the slide line.

[2] For interpretation of color in Figs. 1–14, the reader is referred to the web version of this article.

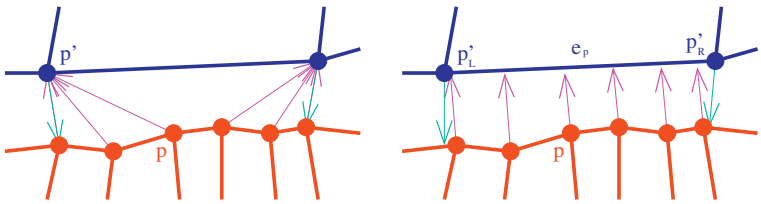

Fig. 3. (a) Point-to-point interaction where many points (p) can interact with one point from the opposite side (p'). (b) Interpolated interaction where points interact with edge e_p, its left and right points denoted by p'_L and p'_R respectively.

ratios are present on each side of the slide line, so the original approach is unlikely to be suitable for problems with high local curvature. This is caused by interaction of several points with a particular point from the opposite side, causing the set of points behaving similarly, while the very next point interacting with a neighboring point from the other side behaves in a significantly different way, as shown in Fig. 3a. Therefore, we suggest here the interpolated interaction, where all the mentioned quantities from the opposite side of the slide line are interpolated from the adjacent point values. For completeness, let us note that the interpolated interaction is used in practice in various numerical codes, however, not many details are available in open literature. For example, in [5,18], the authors treat the interaction of contact nodes with an edge from the other side in the context of Lagrangian multipliers. In [19], the authors accumulate portions of nodal quantities (such as mass) from several opposite-side nodes. In [20], the nodal quantities are distributed to the opposite-side nodes using weighting by mass fractions. And finally in [11], the authors interpolate scalar quantities and normals of vector quantities while projecting the vector components to the normal direction. Similarly, in the approach suggested here, all quantities are interpolated along the edge, however, each component of vector quantities is interpolated separately.

In the point-to-point interaction, a closest point p' from the opposite side has to be determined for any point p on a slide line. In the interpolated interaction, an edge e_p belonging to the opposite side of the slide line and interacting with p has to be determined. Let us note that we reuse the information about the closest point p', and e_p is always one of the slide line edges connected to p'. The relative position of p on e_p is found by the standard projection formula

$$\alpha_p^{e_p} = \max\left(0, \min\left(1, \alpha_p^{e_p,\dagger}\right)\right), \tag{25}$$

$$\alpha_p^{e_p,\dagger} = \frac{(x_p - x_{p'_L})(x_{p'_R} - x_{p'_L}) + (y_p - y_{p'_L})(y_{p'_R} - y_{p'_L})}{\|p'_R - p'_L Vert}, \tag{26}$$

where p'_L and p'_R denote the left and right vertexes of e_p. This situation is shown in Fig. 3b. The interpolation of, for example, mass is then performed by a linear function

$$m_{p'} = m_{p'_L} + \alpha_p^{e_p}(m_{p'_R} - m_{p'_L}), \tag{27}$$

so the value is different for each node interacting with e_p and smoothly changes from $m_{p'_L}$ to $m_{p'_R}$ along the edge, making the interaction more continuous.

Similarly, as shown in (27) for nodal mass, the remaining nodal quantities from the opposite side of the slide line are interpolated in the same way, using the same pre-computed $\alpha_p^{e_p}$ parameters. These are: nodal mass $m_{p'}$, characteristic length $a_{p'}$, nodal normals $\hat{c}_{p'}$, and nodal force $\vec{F}_{p'}$ in contact force (16), the same quantities with p subscript instead of p' in contact force (17), and normals $\hat{c}_{p'}$ and velocities $\vec{v}_{p'}^{n+1,\dagger}$ and $\vec{v}_{p'}^{n}$ in the slave velocity update (19). The vector quantities are interpolated component by component, while the interpolated normals are re-normalized to be unit vectors again. This approach leads to a significant improvement of the staircase-shape problem, see Figs. 8a and 11b.

5. Numerical surface tension

In many tests containing sliding, we can observe the evolution of the Kelvin–Helmholtz instability caused by the shear of different density fluids along each other which can eventually cause the failure of the simulation. This situation can be caused by real physics or wrong model, which is the case for example for gasses, where the disturbance of the interface can be the consequence of the missing model for fluid mixing. In simulations of solids, this problem is typically avoided by introducing a model for material stress/strain, such as [19,21], which causes the material to behave more rigidly; the instability modes are suppressed. We have decided to adopt the technology of numerical surface tension for interface stabilization which is most adequate for description of behavior of liquids. In the formulation of slide line treatment using the Lagrangian multipliers or the penalty method, one can stabilize the interface by an inherited stabilization parameter [7]. Alternative surface stabilization techniques involve for example the viscous interface dumping described in [22].

In our approach, we incorporate the surface tension effect in the form of tension forces in a similar manner, as described in [23]. Let us emphasize here that (contrary to [23]) these forces in our approach do not represent real physical surface tension, it is only a numerical technique for stabilization of a slide line.

The numerical surface tension force acting from zone z on point p, is constructed as

$$\vec{F}_{zp}^{\mathrm{NST}} = s_p \sigma_{zp} \kappa_p \hat{c}_p, \tag{28}$$

where the sign s_p defines the orientation of the force, σ_{zp} represents the pressure gradient in the interface normal direction, κ_p represents the local curvature of the slide line, and the nodal unit normal $\hat{c}_p$ defines the direction of the surface tension force. Due to $\hat{c}_p$ term, the numerical surface tension force only acts in the direction normal to the slide line, no tangential component exists. $\vec{F}_{zp}^{\mathrm{NST}}$ can be incorporated into the subzonal pressure forces $\vec{F}_{zp}$, and have to be included through this force into the slide line contact forces $\vec{G}_p$.

The orientation of the numerical surface tension force is defined as

$$s_p = \begin{cases} -1 & \text{for } \alpha_p \in \langle 0, \pi) \\ +1 & \text{for } \alpha_p \in \langle \pi, 2\pi \rangle \end{cases}, \tag{29}$$

where α_p stands for the internal angle spanned by the slide line edges attached to p. If the slide line is locally convex from one side, the internal angle is acute, therefore $s_p < 0$, and the node is pulled inside the mesh. In the opposite situation, in case of locally concave mesh from one side of the slide line, α_p is obtuse, so s_p is positive, and the node is pushed outside of the mesh. In both cases, the direction leads to straightening of the slide line segment. Let us also

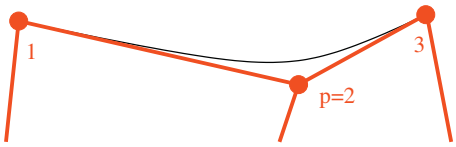

Fig. 4. Part of the mesh attached to a slide line approximated by a Bezier curve. Enumeration of slide line points shown.

present an alternative definition of s_p, avoiding discontinuity in the situation of the straight angle,

$$s_p = \tanh(C(\alpha_p - \pi)). \tag{30}$$

Here, the constant C defines the width of the transition region. Let us note that this definition of s_p is smoother, and moreover, $s_p \approx 0$ for $\alpha_p \approx \pi$ what makes the whole numerical surface tension machinery more robust.

The term σ_{zp} represents the pressure gradient in the vicinity of the slide line. As the pressure force $\vec{F}_{zp}$ is computed using (8), the pressure gradient can be approximated by it. As we are only interested in the size of the pressure gradient in the direction normal to the slide line, which can be computed as

$$\sigma_{zp} \approx \nabla p_{zp} = \left|\vec{F}_{zp} \cdot \hat{c}_p\right|. \tag{31}$$

The last term which we need to define is the local curvature of the slide line κ_p. We compute the curvature in point p as the maximum curvature of a Bezier curve defined by p and its two neighbors in the slide line, as shown in Fig. 4. The Bezier curve is described by the following parametric formula

$$x(t) = (1-t)^2 x_1 + 2t(1-t)x_2 + t^2 x_3, \tag{32}$$

$$y(t) = (1-t)^2 y_1 + 2t(1-t)y_2 + t^2 y_3, \tag{33}$$

where $x_{1,2,3}$ and $y_{1,2,3}$ are the coordinates of the nodes as enumerated in Fig. 4, and where the parameter $t \in \langle 0, 1\rangle$. The curvature is defined by the standard formula

$$\kappa_p(t) = \frac{|\, x'y'' - y'x'' \,|}{\sqrt{\left(x'^2 + y'^2\right)^3}}, \tag{34}$$

where the $'$ symbol represents the derivative with respect to t, and can be computed analytically. The maximum curvature $\kappa_p = \max_{t\in\langle 0,1\rangle} \kappa_p(t)$ is found by the golden section search.

In certain configurations (typically when slide line edges of very different lengths are connected to p), this approach can produce excessive numerical surface tension force due to possibly unbounded value of curvature κ_p. To fix this problem, we have adopted the following limiting approach. If the numerical surface tension force $\vec{F}^{\mathrm{NST}}_{zp}$ is too big compared to the hydrodynamic pressure force $\vec{F}_{zp}$, we perform limiting to a certain amount of $\vec{F}_{zp}$,

$$\vec{F}^{\mathrm{NST,lim}}_{zp} = \beta \frac{\|\vec{F}_{zp}\|}{\|\vec{F}^{\mathrm{NST}}_{zp}\|} \vec{F}^{\mathrm{NST}}_{zp}. \tag{35}$$

In practical simulations, we use 10% of the pressure force, i.e. $\beta = 1/10$. Next to it, in practical calculations, one may want to incorporate a switch which enables the numerical surface tension force only if s_p changes its sign in the neighborhood of p. This avoids the straightening of the slide line in smooth regions, while it still prevents its pathologic zigzagging.

Let us note that the numerical surface tension mechanism can change physics in the vicinity of the interfaces by straightening the material interface. This straightening eliminates the development of instabilities on the interface, which may or may not be desirable. The usage of this mechanism therefore depends on a particular simulation. For problems containing pure sliding of materials along each other, the numerical surface tension mechanism helps to stabilize the interface and increases robustness of the calculation. On the other hand, for simulations of instabilities, the numerical surface tension mechanism can eliminate the growth of the instability completely, so this mechanism is not suitable at all. In general, this mechanism should be used only as little as possible to avoid excessive interface straightening.

6. Numerical examples

In this section, we present several numerical examples to demonstrate the behavior of the original method and its comparison with the improved method combining the interpolated interaction and the numerical surface tension.

6.1. Pure sliding

The first numerical example is a sanity check testing the robustness of the methods and their ability to maintain straight material interface. The $\langle 0, 2\rangle^2$ computational domain is split in the middle by a vertical slide line into two different non-uniform computational meshes, with different mesh resolution in each quadrant of the domain [24]. The initial meshes are shown in Fig. 5a. All fluid quantities are constant in the entire domain except the vertical velocity which is $+0.02$ in the left mesh and -0.02 in the right mesh. The final time is $t = 10$.

All methods keep the straight slide line exactly, no violation occurs, as shown in Fig. 5b. This is confirmed by the ΔW energy discrepancy which is zero up to machine accuracy for all methods. Due to non-equidistant nature of the meshes, this test checks the infrastructure of the slide line framework, especially the mechanism of scaling the contact forces to the segment size across the interface by the parameter a_p.

6.2. Saltzman-like piston

Another sanity check is inspired by the standard Saltzman piston problem, however, a standard uniform orthogonal mesh is used instead of the skewed Saltzman mesh. The whole $\langle 0, 1\rangle \times \langle 0, 0.1\rangle$ domain is covered by a 100×10 mesh which is split in the middle of the domain by a horizontal or vertical slide line, as shown in Fig. 6a and b. The fluid has a unit density and zero (in practice, 10^{-8} is used) pressure, and it is static except the left boundary which is moving with unit velocity representing a piston compressing the fluid. The value of $\gamma = 5/3$ is used everywhere, the final time is $t = 0.98$. The whole problem is rotated by a non-trivial angle $\pi/6$ to avoid interference with the axes directions. (The non-rotated problem produced perfect results for all methods and is consequently skipped.)

Interesting parts of the final computational meshes are shown in Fig. 6c and d. No difference among the methods can be visually observed, so only images for the interpolated interaction with the numerical surface tension are presented. As we can see, the 1D nature of the problem is preserved perfectly in both cases for all methods. For the horizontal slide line test, no discrepancy occurs at all, the ΔW energy discrepancy is zero up to machine accuracy for all methods. In case of vertical slide line, small discrepancy appears for all methods ($\Delta W \approx 10^{-9}$), and a small oscillation in density shows up close to the slide line. This is caused by the shock wave passing the interface and consequent velocity correction, which did not appear in case of horizontal slide line as no velocity correction was performed due to normal direction of the slide line and the shock wave. However, the 1D symmetry as well as the shock wave velocity is not affected.

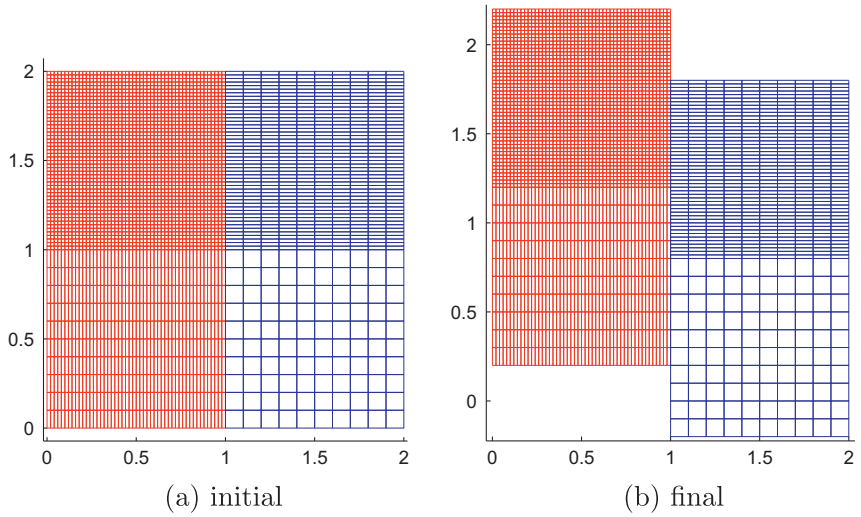

Fig. 5. (a) Initial 40×50 and 10×50 meshes of the pure sliding sanity check. (b) Final meshes.

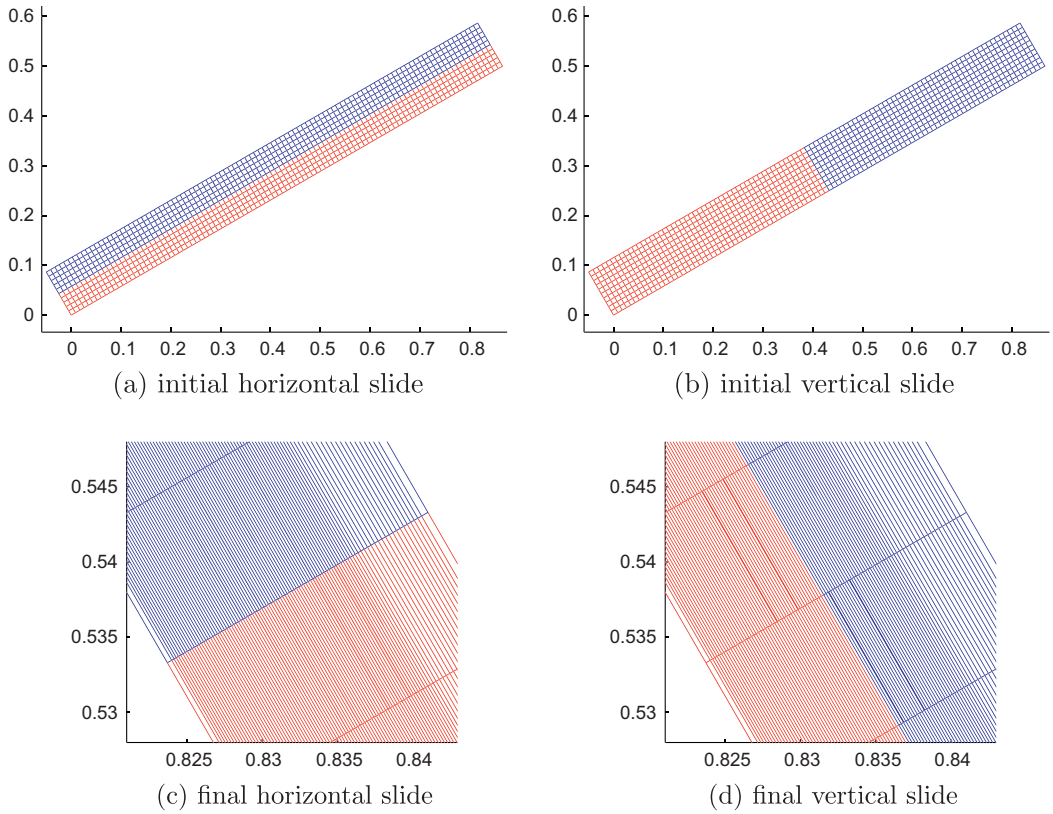

Fig. 6. Saltzman-like piston with a slide line: initial (a) and (b) and final (c) and (d) meshes for Saltzman-like piston problem separated by a horizontal (a) and (c) and vertical (b) and (d) slide line.

6.3. Sliding rings

In this section, we describe a problem in which an inner low-density ring slides along an outer heavier ring. This problem is similar to the pure sliding test presented in Section 6.1, however, this is not just a sanity check any more as real hydrodynamic effects take place here due to the centrifugal forces. Both initial meshes contain 100×20 computational cells. The outer mesh uniformly spans from $-\pi/4$ to $5/4\pi$ in the angular direction and from 2 to 3 in the radial direction. The inner mesh spans from 0 to $\pi/2$ in the angular direction and from 1 to 2 in the radial direction, so there is a $1/3$ aspect ratio between the meshes. The initial meshes are shown in Fig. 7. Both meshes contain initially uniform unit pressure, the inner (slave) mesh with uniform unit density slides by a unit angular velocity along the static outer (master) ring with density 10^4. The simulation stops at time 0.65, just before the original method fails.

The results of the simulations are shown in Fig. 8. The original method provides significantly worse results when compared with the improved method what is caused by the staircase-shape problem due to a different aspect ratio of the meshes, as described in Section 4. This problem propagates though the computational

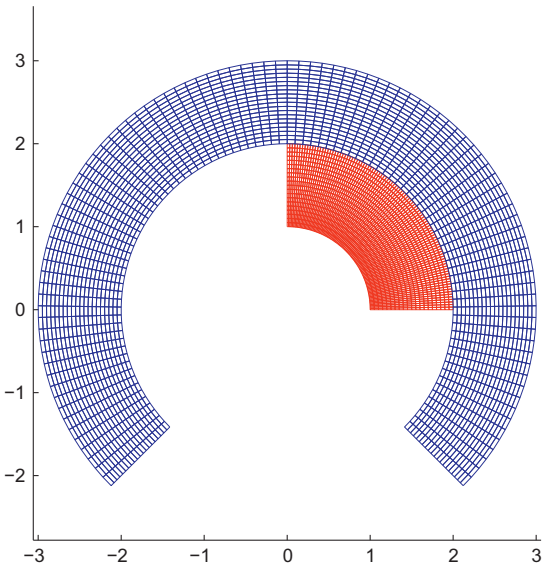

Fig. 7. Initial meshes for sliding rings problem separated by a circular slide line.

mesh and can be seen as strong disturbances in the mesh and also in the density (and other quantities) profiles. The interpolated interaction helps significantly and the simulation can continue. As the slide line shape is maintained smooth in this case, the numerical surface tension does not change the behavior significantly due to low curvature term κ_p in formula (28).

Note a significant inter-penetration in the original method, which is eliminated by the interpolated interaction. As for the energy discrepancy due to velocity correction, it is of the order of 10^{-3} for the original method, and one order of magnitude lower for the improved methods. Clearly, this problem demonstrates the ability of the interpolated interaction mechanism to suppress the staircase shape problem and stabilize the interface.

6.4. Explosion with sliding

In this section, we demonstrate the behavior of the methods on a more complex test coming from Ref. [15], representing a realistic problem including a shock wave along the slide line, a shock wave in the direction normal to the slide line, and sliding at the same time. The computational domain $\langle 0, 1\rangle \times \langle 0, 0.5\rangle$ is divided by a horizontal slide line into two static uniform meshes of 100×25 cells. The lower (slave) mesh has a unit density, pressure is 20 in cells left from $x = 0.05$, and $2/3 \times 10^{-8}$ right from it. This high pressure generates a shock wave moving to the right. The upper (master) mesh has density 10 and pressure $2/3 \times 10^{-8}$ everywhere. The value of $\gamma = 5/3$ is used in the entire domain. The initial configuration is shown in Fig. 9a. The simulation is stopped at time $t = 0.4$.

Fig. 9b presents the simulation performed on a single computational mesh without a slide line. Note a significant mesh distortion along the material interface due to shear flow, causing high numerical error and eventually degeneracy of the computational time-step. The results of the simulations with a slide line are shown in Fig. 10. All methods provide better results than the one-mesh approach, the meshes slide along each other, and the horizontally moving shock wave is nicely captured as no mesh distortion is present. The vertically-moving shock waves from the original method and the improved method are almost identical in the density pictures, when numerical surface tension is added, it is slightly flatter. The void region in the left part of the mesh is bigger for the original

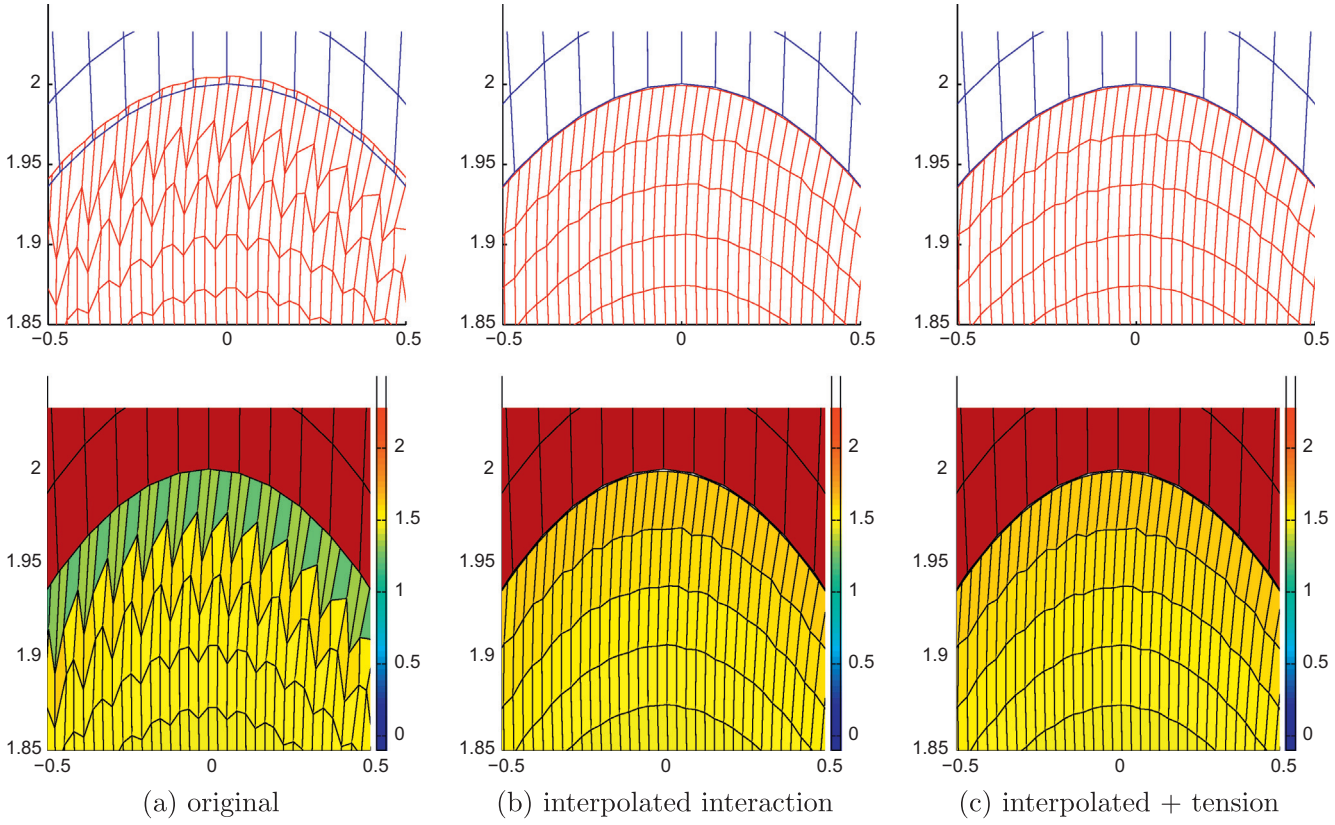

Fig. 8. Zoom to the interesting part along the slide line for the sliding rings problem (aspect ratio not preserved). Comparison of computational meshes and density field for the original approach and the improved method with interpolated interaction and surface tension shown.

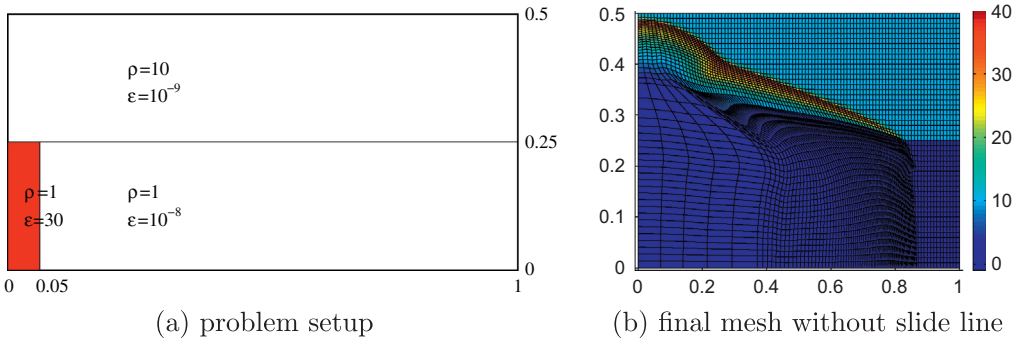

Fig. 9. Problem of explosion with sliding. (a) Initial data. (b) Simulation on a single mesh with no slide line present.

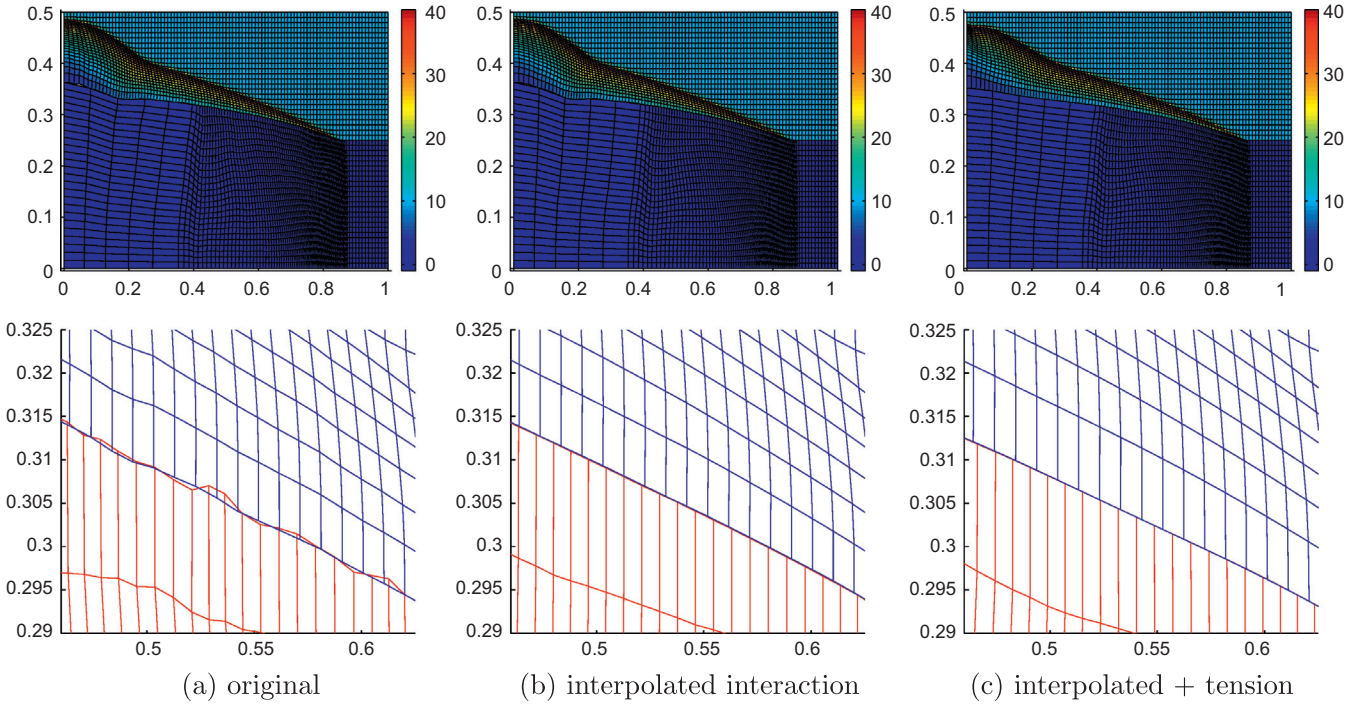

Fig. 10. Results for problem of explosion with sliding. Density profiles and zoom to the slide line regions (aspect ratio not preserved) are shown for the original approach and the improved method with interpolated interaction and surface tension.

approach, it is reduced by interpolated interaction, and almost eliminated by adding the numerical surface tension. The density profile of the original method is almost identical with the profile presented in [15].

When looking at the mesh segments along the slide line in the post-shock region for the original method, one can see the development of serious disturbances due to the staircase-shape problem again. This problem is significantly reduced by switching to the interpolated interaction again (Fig. 10b and c). As for the energy discrepancy, it is comparable for all methods for this problem, $\Delta W = 8.8 \times 10^{-3}$ for the original method, it drops to $\Delta W = 7.1 \times 10^{-3}$ for the interpolated interaction, and increases slightly to $\Delta W = 7.5 \times 10^{-3}$ when numerical surface tension is added.

6.5. Bullet in channel

This test is inspired by real physical experiments, dealing with ablative acceleration of dense plasma in a channel [25], which were performed at the Prague Asterix Laser System (PALS). The initial mesh is shown in Fig.11a. The $\langle 0, 2\rangle \times \langle 0, 10\rangle$ computational domain is split by a vertical slide line. The right (master) part is covered by a initially static uniform mesh of 20×100 cells with density equal to 10 and pressure 1, representing the channel boundary. The left (slave) part of the domain represents the inside of the channel. It is divided into three parts: the uppermost air (5 cells between $y = 9$ and $y = 10$), the bullet (90 cells between $y = 8$ and $y = 9$), and air (5 cells between $y = 0$ and $y = 8$). The density is 1 in the heavy bullet and 0.1 in the air. The air is initially static, the bullet moves down with the velocity 7. The value of $\gamma = 5/3$ is used in the entire domain. The simulation stops at time $t = 1.17$, just before the original approach fails.

Due to the bullet motion, the lower air is compressed, the pressure here is increased, and the slide line deforms due to the developed pressure gradient. This problem involves a strong difference in aspect ratios across the slide line, which drives the staircase-shape problem very strongly.

Fig. 11b–d presents the situation in a very early stage of the simulation at $t = 0.1$. The original method suffers from severe distortions. We can clearly identify sets of points from the master side interacting with the particular points on the slave side. On the

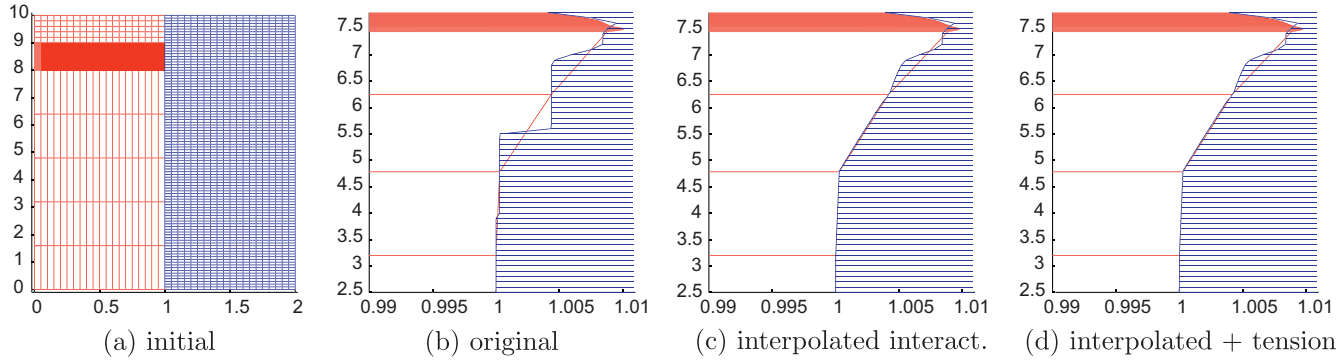

Fig. 11. Computational meshes for the bullet in a channel test at $t = 0.1$. (a) Initial mesh of the bullet in a channel test. (b)–(d) Comparison of the original approach with the improved method with interpolated interaction and surface tension.

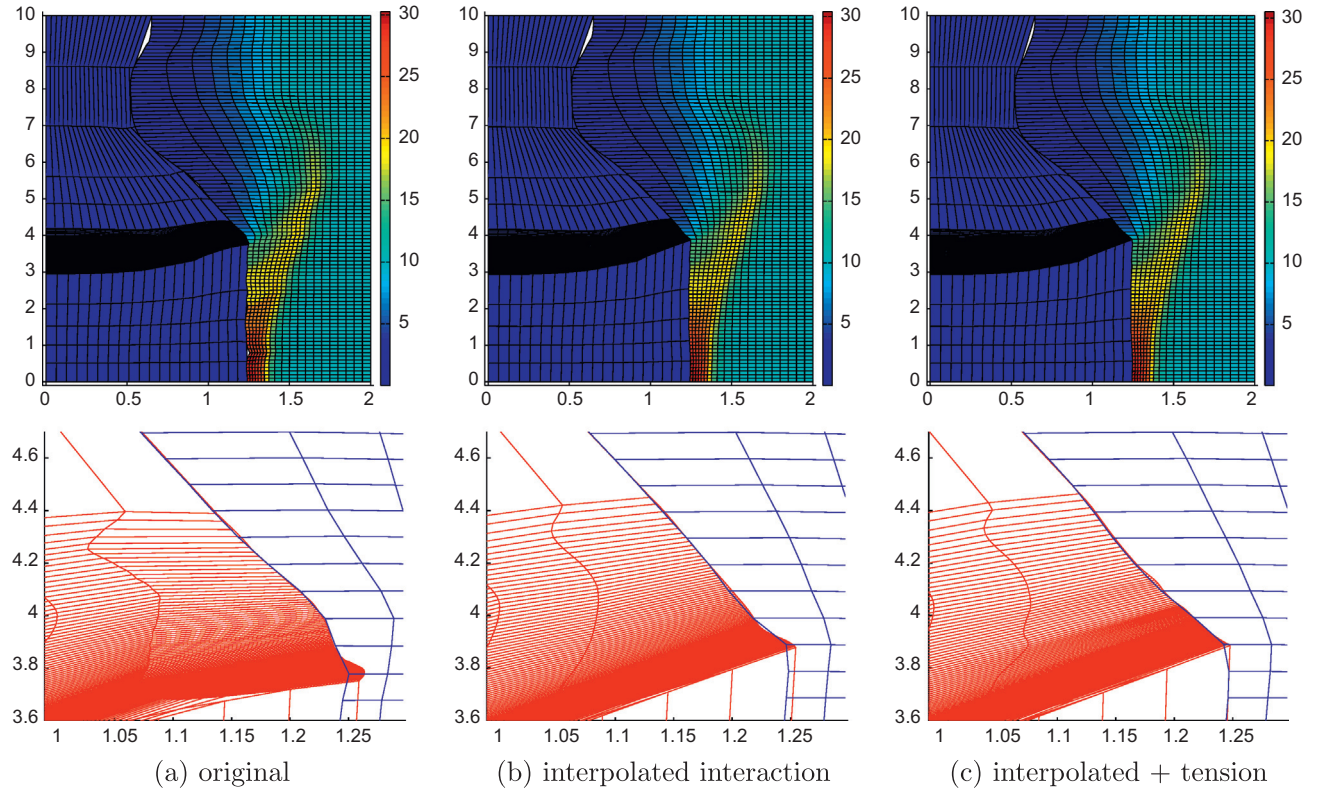

Fig. 12. The density profiles in the entire domain and mesh segments in the interesting region close to the slide line (aspect ratios not preserved). Comparison of the original approach with the improved method with interpolated interaction and surface tension.

other hand, the interpolated interaction demonstrates reasonable shift of the master nodes along the edges of the slave boundary. At this early stage of the simulation, the numerical surface tension does not have any significant influence as the shape of the slide line is still smooth.

Fig. 12 presents the density field in the entire domain at the final time $t = 1.17$, as well as the part of the meshes close to the slide line. The largest voids between the meshes appear in the case of the original method, but the global picture (bullet shape, shock wave position, etc.) is the same for all methods. Looking at the mesh part along the slide line, one can notice the significant inter-penetration when the original method is used, which is reduced by the interpolated interaction and almost eliminated by adding the numerical surface tension. The ΔW energy discrepancy is comparable for all methods.

6.6. Sedov explosion with an interface

In this section, we demonstrate the symmetry violations introduced by the slide line machinery for an initially symmetric problem. This problem resembles the standard Sedov point explosion problem on polar computational mesh. The initial mesh covers the radius $r \in \langle 1/100, 1.1\rangle$ and the angular interval is $\theta \in \langle 0, \pi/2\rangle$. Small radius around the origin prevents the degenerate points to appear. The computational mesh is split by a slide line at $r = 1/2$, where the outer mesh acts as its master side. Both meshes have 20 computational cells in the radial direction. The outer mesh contains 100 cells while the inner mesh has only 31 cells in the angular direction, so the nodes do not coincide at the slide line. The entire domain contains unit-density zero-pressure gas (in practice, $p = 10^{-10}$ is used) with $\gamma = 1.4$, except the innermost ring

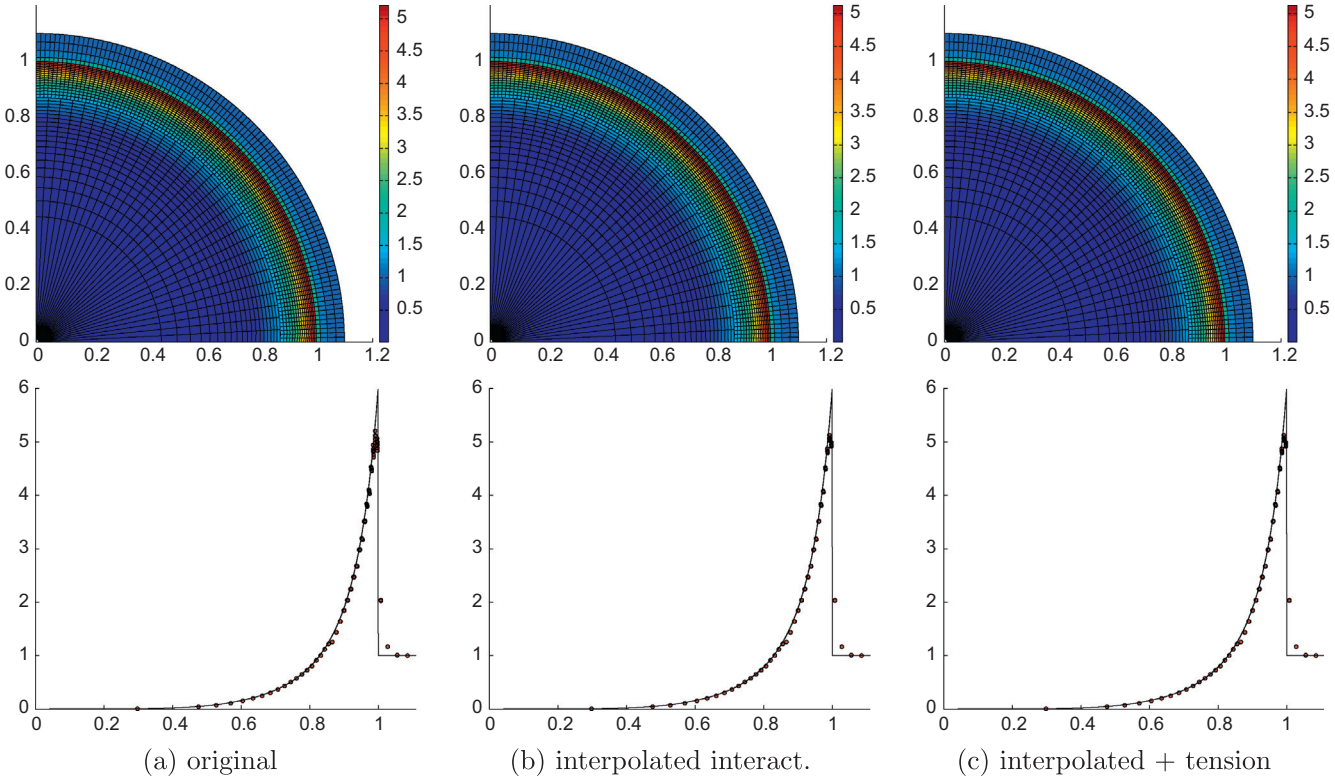

Fig. 13. The density profiles in the entire mesh (upper figures) and scatter plot of all cell densities as a function of radius (lower figures) against the analytic solution for the original approach and the improved method with interpolated interaction and surface tension.

of cells where the value of $p = 114.359$ is used. This value is found to exactly correspond to the standard version of the Sedov problem presented for example in [26]. The final time of the simulation is $t = 1$.

When this problem is solved on a single mesh without any slide line, the solution preserves its symmetry up to machine accuracy. We measure the non-symmetry as the ratio of the angular momentum and the total momentum. The solutions when a slide line is present is shown in Fig. 13. As we can see, small decrease in the density value is visible at the slide line (around $r = 0.9$ in Fig. 13) for all slide line treatments. Let us note this dip is not present for single mesh simulation and probably originates from the energy discrepancy due to velocity correction at the slide line. However when meshes with termination lines or hanging nodes are employed, the preservation of symmetry becomes tricky [27] especially when nodes on both sides do not coincide as in our case. Even visually, we can observe some non-symmetry of the solution between the slide line and the shock front, especially for the original approach. The relative momentum in the angular direction is 4.008×10^{-4} for the original approach, 3.230×10^{-4} for the interpolated interaction, and 3.223×10^{-4} for the interpolated interaction with the surface tension. The ΔW energy discrepancy is comparable for all methods. Let us note that for this problem, the surface tension switch mentioned in Section 5, which disables the tension in smooth regions was used. Without this switch, the surface tension force tries to make the slide line straight and symmetry of the problem is violated significantly.

6.7. Rayleigh–Taylor instability with sliding

In this section, we want to analyze the influence of the slide line treatment on the growth rate of the Rayleigh–Taylor instability problem [28] against the theoretical rate. The initial configuration is exactly adopted from Ref. [28]. This simulation is performed on a single 100×600 mesh without any slide line, and also on two 100×300 meshes separated by a slide line. The upper mesh containing the high density fluid acts as master in these calculations.

In Fig. 14, we present the growth rates of the instability and their comparison with the analytic rate [28] during the linear phase of the instability growth. First of all, we can see that the simulation without the slide line follows almost exactly the analytic curve until $t = 0.6$. After that, the shear along the fluid interface decelerates the growth due to interface nodes belonging to both fluids and stick to each other. This problem is improved by introducing a slide line separating the fluids, so the interface nodes are freely moving along the interface, without further restrictions

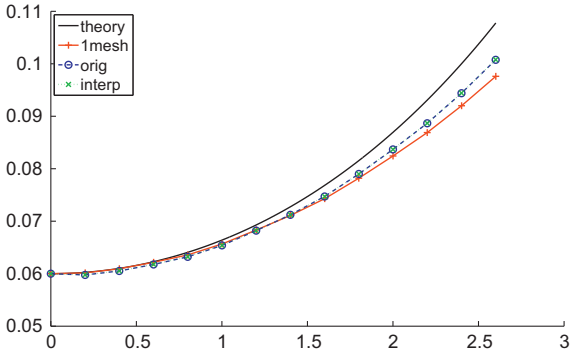

Fig. 14. Comparison of analytic growth rate (black) of the Rayleigh–Taylor instability with the numerical calculations performed on single mesh (red), and on two meshes separated by a slide line treated by original approach (blue) and the interpolated interaction (green). Blue and green curves are superimposed. (For interpretation of the references to color in this figure legend, the reader is referred to the web version of this article.)

from the opposite side. At time $t = 1.3$, the growth rates in the calculations with the slide line exceed the single mesh results, better corresponding to the theoretical growth and the results from Ref. [28].

We can see that the results of the original method almost coincide with the results of the interpolated interaction. Let us note that the result with numerical surface tension is omitted here as it is not appropriate for this kind of problem. The numerical surface tension mechanism is designed to stabilize the interface and eliminate the instability, so the instability amplitude decreases instead of increasing according to theory.

7. Conclusions

We have reviewed the slide line treatment from Ref. [15] in the staggered Lagrangian framework. On the selected numerical examples, we have demonstrated some pathologies of this method in the case of different aspect ratios of the computational meshes. This problem can be described as staircase-shape due to similar interaction of several mesh nodes from the finer side of the slide line with a particular node in the coarser side, and just next to them, another set of points interacting with a neighboring node in the coarser side. We describe the technique of interpolated interaction which eliminates this problem.

A second problem is the development of Kelvin–Helmholtz instability in the vicinity of the slide line due to a shear flow in this region. We suggest here a numerical surface tension formulation which suppresses this problem and stabilizes the slide line by making it more rigid. This technique is however devoted to cure hydrodynamical instability. Obviously if such instabilities must be kept or if more advanced material strength model is used then this technique should not be employed.

On selected numerical examples, we demonstrate the advantages of the improved methods by comparison with the original approach. We show here that the interpolated interaction provides a much more regular shape of the slide line than the original method. It is also demonstrated that the numerical surface tension process does not affect the slide line shape when it is reasonably smooth, but starts to stabilize it when perturbations appear. In all tests shown here, the improved method provides better results than the original method [15].

Acknowledgments

The authors thank E.J. Caramana for clarifications of many details and discussion of many issues related to this topic. They also thank the reviewers for their valuable comments and suggestions that improved the quality of the paper. This research was supported in parts by the Czech Ministry of Education Grants MSM 6840770022, MSM 6840770010, MEB021020, and LC528, the Czech Science Foundation Project P201/10/P086, and the Czech Technical University Projects SGS10/299/OHK4/3T/14 and RVO 68407700. The authors warmly thank the support of the French embassy in Prague, Czech Republic under the Vltava program, which has provided the conditions for this work to reach maturity.

References

[1] Limpouch J, Liska R, Kuchařík M, Váchal P, Kmetík V. Laser-driven collimated plasma flows studied via ALE code. In: 37th EPS conference on plasma physics. European Physical Society; 2010. p. P4.22. ISBN 2-914771-62-2.
[2] Kuchařík M, Liska R, Limpouch J, Váchal P. ALE simulations of high-velocity impact problem. Czech J Phys 2004;54(Suppl. C):391–6.
[3] Zukas Jonas A, editor. Introduction to hydrocodes. Studies in applied mechanics, vol. 49. Elsevier; 2004.
[4] Benson DJ. Computational methods in Lagrangian and Eulerian hydrocodes. Comput Methods Appl Mech Eng 1992;99(2–3):235–394.
[5] Wriggers P. Computational contact mechanics. second ed. Springer-Verlag; 2006. ISBN 10 3-540-32608-1.
[6] Zywicz E, Puso MA. A general conjugate-gradient-based predictor-corrector solver for explicit finite-element contact. Int J Numer Methods Eng 1999;44(4):439–59.
[7] Weyler R, Oliver J, Sain T, Cante JC. On the contact domain method: a comparison of penalty and Lagrange multiplier implementations. Comput Methods Appl Mech Eng 2012;205–208:68–82.
[8] Wilkins ML. Calculation of elastic-plastic flow. Technical report UCRL-7322, California. Univ., Livermore, Lawrence Radiation Lab.; 1963.
[9] Wilkins ML. Computer simulation of dynamic phenomena. Scientific computation. Springer; 1999.
[10] Burton DE. Advances in the free-lagrange method including contributions on adaptive gridding and the smooth particle hydrodynamics method. Lecture notes in physics, vol. 395. Springer; 1991. p. 267–76 [Chapter Free-Lagrange Advection Slide Lines], ISBN 978-3-540-54960-4.
[11] Barlow AJ, Whittle J. Mesh adaptivity and material interface algorithms in a two dimensional Lagrangian hydrocode. Chem Phys Rep 2000;19(2):15–26.
[12] Dawes AS. A three-dimensional contact algorithm for sliding surfaces. Int J Numer Methods Fluids 2003;42(11):1189–210.
[13] Bourago NG. A survey on contact algorithms. In: Ivanenko SA, Garanzha VA, editors. Proceedings of workshop grid generation: theory and applications. Moscow: Computing Centre of RAS; 2002.
[14] Caramana EJ, Burton DE, Shashkov MJ, Whalen PP. The construction of compatible hydrodynamics algorithms utilizing conservation of total energy. J Comput Phys 1998;146(1):227–62.
[15] Caramana EJ. The implementation of slide lines as a combined force and velocity boundary condition. J Comput Phys 2009;228(11):3911–6.
[16] Caramana EJ, Shashkov MJ, Whalen PP. Formulations of artificial viscosity for muti-dimensional shock wave computations. J Comput Phys 1998;144(2):70–97.
[17] Caramana EJ, Shashkov MJ. Elimination of artificial grid distortion and hourglass-type motions by means of Lagrangian subzonal masses and pressures. J Comput Phys 1998;142(2):521–61.
[18] Carpenter NJ, Taylor RL, Katona MG. Lagrange constraints for transient finite element surface contact. Int J Numer Methods Eng 1991;32(1):103–28.
[19] Hallquist JO, Goudreau GL, Benson DJ. Sliding interfaces with contact-impact in large-scale Lagrangian computations. Comput Methods Appl Mech Eng 1985;51(1–3):107–37.
[20] Zhong ZH. On contact-impact problems. PhD thesis, Linkoping University, Linkoping, Sweden; 1988.
[21] Weseloh WN, Clancy SP, Painter JW. PAGOSA physics manual. Technical report. Los Alamos National Laboratory; 2010 [LA-14425-M].
[22] ABAQUS 6.10 Analysis User Manual, vol. V. Dassault Systemes; 2010.
[23] Francois MM, Cummins SJ, Dendy ED, Kothe DB, Sicilian JM, Williams MW. A balanced-force algorithm for continuous and sharp interfacial surface tension models within a volume tracking framework. J Comput Phys 2006;213(1):141–73.
[24] Dobrev VA, Ellis TE, Kolev TzV, Rieben RN. Curvilinear finite elements for Lagrangian hydrodynamics. Int J Numer Methods Fluids 2011;65(11–12):1295–310.
[25] Badziak J, Borodziuk S, Pisarczyk T, Chodukowski T, Krousky E, Masek K, Skala J, Ullschmied J, Rhee Y-J. Highly efficient acceleration and collimation of high-density plasma using laser-induced cavity pressure. Appl Phys Lett 2010;96(25):251–502.
[26] Galera S, Maire P-H, Breil J. A two-dimensional unstructured cell-centered multi-material ALE scheme using VOF interface reconstruction. J Comput Phys 2010;229(16):5755–87.
[27] Loubère R, Caramana EJ. The force/work differencing of exceptional points in the discrete compatible formulation of Lagrangian hydrodynamics. J Comput Phys 2006;216(1):1–18.
[28] Fung J, Francois M, Dendy E, Kenamond M, Lowrie R. Calculations of the Rayleigh–Taylor instability: RAGE and FLAG hydrocode comparisons. In: Proceedings of NECDC06; 2006.